

Rational Chebyshev Spectral Transform for the dynamics of high-power laser diodes

J. Javaloyes*

Universitat de les Illes Balears, C/ Valldemossa, km 7.5, E-07122 Palma de Mallorca, Spain

S. Balle

Institut Mediterrani d'Estudis Avançats, CSIC-UIB, E-07071 Palma de Mallorca, Spain

This manuscript details the use of the rational Chebyshev transform for describing the transverse dynamics of high-power laser diodes, either broad area lasers, index guided lasers or monolithic master oscillator power amplifier devices. This spectral method can be used in combination with the delay algebraic equation approach developed in [1], which allows to substantially reduce the computation time. The theory is presented in such a way that it encompasses the case of the Fourier spectral transform presented in [2] as a particular case. It is also extended to the consideration of index guiding with an arbitrary profile. Because their domain of definition is infinite, the convergence properties of the Chebyshev Rational functions allow handling the boundary conditions with higher accuracy than with the previously studied Fourier method. As practical examples, we solve the beam propagation problem with and without index guiding: we obtain excellent results and an improvement of the integration time between one and two orders of magnitude as compared with a fully distributed two dimensional model.

I. INTRODUCTION

An increasing demand for high-power and high-brightness laser diodes [3] stems from applications such as solid state and fiber laser pumping, telecommunications, remote sensing, medicine or material processing. Laser diodes offer high wall-plug efficiency, reliability, long lifetime, relatively low investment costs and a small footprint, but their output power is limited because of Catastrophic Optical Damage (COD) of the facets. The most direct path to increase the output power is to reduce the power density on the facets, which can be achieved by increasing the lateral size of the diode up to several hundreds of μm . These so-called Broad-Area Laser Diodes (BALDs) have allowed to obtain output powers $\sim 10\text{W}$ in CW operation [4]. The increase in power, however, usually implies a degradation of the optical quality of the beam: the emission profile in the lateral dimension varies with current due to thermal lensing and spatial hole burning in the carrier density. These phenomena result in high M^2 factors that limit the ability to focus the beam [5], and they might even lead to chaotic filamentation [6, 7] of the beam. In fact, when several high order modes are usually present, the emission profile is usually not stationary [8].

In order to achieve high-output power with an improved beam quality from laser diodes, two main approaches have been pursued, the monolithic Master-Oscillator Power Amplifier (MOPA) and the Tapered Laser (TL), although alternative options do exist [9–14]. Such TLs have an active region of varying width along the propagation direction [15]; usually, their design includes a relatively short ($\sim 500\ \mu\text{m}$ long) straight region that supports a single lateral mode with a longer ($\sim 1-2$

mm) section whose width expands significantly, reaching $\sim 100\ \mu\text{m}$ at the output facet. The straight region is intended to provide spatial mode filtering, but the longitudinal mode structure of the device is defined by the total length of the optical cavity. The structure of MOPA [16] devices is similar to TLs. They integrate a low-power, conventional single-mode laser diode (which provides an optical beam of good quality) with a semiconductor optical amplifier for boosting the power level; in this case, however, the longitudinal mode spectrum is intended to be determined by the short section only, which requires using anti-reflection coatings of very high quality on the output facet. In both cases, one of the major challenges is the design of the connection of the two sections in order to minimize the onset of multiple peaks in the lateral far and near field profiles, specially at high currents, where the optical spectrum also tends to broaden. Often, angled index steps known as beam spoilers are included in this region in order to improve the spatial filtering effect of the short straight region.

The complexity of these devices has stimulated the development of sophisticated models and simulation tools that can guide the design of these devices for improving their performances [17–19]. These models must include not only the structure of the passive cavity (through the spatial distribution of dielectric constants) but also the state of the active region through the material's response function that depends on the spatial distribution of carriers and temperature [20]. Indeed, it is crucial to reach a self-consistent solution for the electrical, thermal and optical problems in order to correctly describe the behavior of these devices; however, the different time scales involved in these processes may allow to treat each of them separately, imposing self-consistency at the end.

The optical simulation module has to solve for the field and carrier distribution in the device. The three-dimensional nature of the problem is often reduced to only the lateral and longitudinal directions by invoking

*Electronic address: julien.javaloyes@uib.es

the effective index approximation in the dimension perpendicular to the active region plane. Time-independent models based on Helmholtz equation have been developed in order to determine the lateral mode structure of these devices. In this approach, no a priori assumptions are made about either the field profile or its characteristics, and the problem is solved on a spatial grid with sub-wavelength resolution; given the large size of the device, this is a very memory-expensive approach. A less-demanding approximation is provided by Beam-Propagation Methods [21–23], where the longitudinal field profile is decomposed into unidirectional traveling waves, the amplitudes of which are assumed to vary slowly along the cavity. This Slowly-Varying Amplitude Approximation (SVA) allows to relax the discretization requirements, and provides a good approximation to the modal profile under single-mode operation, including self-focusing of the beam. However, time-independent models cannot deal with dynamical phenomena, like beam filamentation, nor predict the onset of instabilities. For this reason, several time-dependent models have been developed. Most of these models are also based on the decomposition of the intra-cavity field into counter-propagating waves [24–28] in the SVA, differing mainly in the description of the optical response of the material, hence they are generically termed as Traveling-Wave Models (TWMs) [26–28].

The numerical approaches for tackling these problems can be classified as Finite-Difference (FD) methods and spectral or pseudo-spectral methods. FD methods easily allow for the use of non-uniform grids, transparent or radiative boundary conditions can be readily implemented, and they are accurate for high index-contrast geometries. However, the Von Neumann analysis reveals that only the central part of the spectrum, i.e. the shallowest frequencies, are properly advected during the dynamics while another (large) part of the spectrum suffers from severe amplitude and phase deformations, see [29] Chap. 20. Instead, spectral methods do not distort the spectrum because they exactly consider the spatial derivative operators; as a consequence, when seeking for high accuracy smooth solutions, like e.g. the transverse modal structure of a BALD, spectral and pseudo-spectral algorithms may converge to the solution much faster than FD algorithms, due to the so-called “infinite order” or “exponential” convergence [30] of the former.

The most popular spectral method is certainly the Fourier Transform (FT) whose main advantages are to diagonalize the derivative operators and to be achievable via an algorithm of low complexity ($N \log N$, where N is the number of points in the spatial grid [31]) and to be readily available as a quality open source software [32]. In addition, the method of Exponential Differencing [33] combined with the FT spectral method allows to treat exactly the influence of the spatial derivatives operators like diffusion and diffraction over an interval that does not need to be infinitesimal (i.e. say, relatively large temporal or spatial steps can be used). It has been recently

shown [2] that such an exact treatment of diffraction over a large increment can work in synergy with the delay Algebraic Equation (DAE) mapping of TWMs developed in [1]. Such a DAE mapping typically allows for a reduction of the number of degrees of freedom—hence the computation time—between one and two orders of magnitudes, which alleviates the need of complex parallel codes for the simulation of BALD, MOPA and TL devices.

However, the FT spectral method automatically imposes periodic boundary conditions in the lateral direction that are wrong for laser diodes, where the physical boundary conditions for the field amplitude are of the radiative type even for the laterally confined modes that decay exponentially away from the active region. Hence, one is in general forced to consider a sufficiently large transverse domain in which the field is only concentrated in the central stripe and as such, possesses enough space to decay “naturally” to zero and not feel the presence of the wrong boundary conditions. Tapered devices are particularly demanding from this point of view: the need to extend the current strip only over a small part of the numerical domain has to be satisfied even at the exit facet, where the tapered device has its maximal breadth, which then defines the lateral size of the rectangular box. However, an acceptable resolution where the tapered device is the broadest means that at the same time the thinner part may only be resolved by a handful of points. As such, one is forced to use an extremely demanding discretization everywhere in order to properly resolve the narrower part and one ends up with an extremely large rectangular numerical domain composed of a very fine grid in which the active current stripe extend only over a fraction of the rectangle. The inclusion of an absorbing Perfectly Matched Layer (PML) close to the boundary may help to mitigate this problem; however, an abrupt transverse variation of the losses would in principle give rise to a convolution product in the Fourier domain which may render the inclusion of such a PML if not difficult, at least costly from a numerical point of view. Another drawback of the FT spectral method is that its basis functions (plane waves) are not the most adequate for describing the exponential decaying tails of the field outside of the central stripe, which may result in a sub-optimal convergence.

The aforementioned points suggest that a spectral method based upon a set of functions which decay, even weakly, in $x = \pm\infty$ may improve on the convergence properties, as clearly indicated in the discussion at the end of [34]. In addition, a non uniform discretization—with a high density of points in the central stripe where the non linear dynamics occurs, and a low density of points in the outer regions, where the field decays linearly—would represent a clear improvement. These considerations hint toward the use of a different spectral method, namely the Rational Chebyshev Transform (RCT). The RCT devised by Christov consists in a modification of the Chebyshev Transform defined on $x \in [-1, 1]$ onto $x \in [-\infty, \infty]$ by an arctangent map-

ping [35]. The basis consists in a full set of rational fraction function which tends to zero at $x = \pm\infty$ and that are represented over a non uniform mesh of points whose density decreases with the distance from the origin. Such a method solves the aforementioned drawback of the FT method while keeping essentially its good properties, i.e. a simple representation of the spatial derivative, even upon Exponential Differencing [33], and surprisingly enough, a fast $N \log N$ implementation based upon the Fourier transform.

In this work, we discuss how a RCT spectral method over a variable grid following the variations of the current stripe profile along the cavity axis can be implemented for a TWM at a marginal increase in complexity as compared to the FT method developed in our earlier work [2]. We use the TWM developed in previous works[28] generalized to the presence of transverse diffraction and including both index- and gain-guided sections as encountered in the different sections of MOPAs and TLs. Propagation along the axis is solved in time-domain using the DAE formalism [1], which enables using a coarse discretization along the optical axis. The numerical algorithm is formally equivalent for both the RCT and the FT approaches. As such, we present our theory in an unified way where only the precise form of the matrices corresponding to the second derivative, the index guiding and the extra term due to the variable grid differ between the RCT and FT method.

This manuscript is organized as follows. In Section II, we recall the basis of our TWM [28] generalized to the presence of transverse diffraction. We detail in Section III the basic properties of the RCT, and in Section IV the representation in this basis of the second order spatial derivatives and of transverse index guiding. Section V is devoted to the implementation of the DAE transformation using Exponential Differencing [33] and discuss how one must treat the boundary conditions along the longitudinal direction. We detail in particular the many caveats present in the evaluation of the integration weights due to the stiffness incurred by the spectral transformation. We also show how the full two dimensional mesh profile can be reconstructed from the few actives ‘‘slices’’ that remain active with the DAE approach. In Section VI, we exemplify the validity of our approach by studying a variety of cases and comparing the FT and the RCT methods.

II. MODEL

Our model considers a single mode structure in the transverse direction, which is reduced via the effective index approximation. The optical field in the cavity is assumed to be almost TE polarized and it is decomposed into a forward and a backward wave of SVA $E_{\pm}(x, z, t)$. In addition, the carrier density $N(x, z, t)$ in the cavity is decomposed into a quasi-homogeneous term $N_0(x, z, t)$ and a (weak) grating term at half the optical wavelength,

$N_{\pm 2}(x, z, t)$, with $N_{-2}(x, z, t) = N_2^*(x, z, t)$. The instantaneous distributions E_{\pm} , N_0 and $N_{\pm 2}$ in the lateral ($x \in [-\infty; \infty]$) and longitudinal ($z \in [0; L_z]$) direction are described in the paraxial approximation by a TWM [28] extended to include diffraction in the transverse dimension. From the numerical point of view, however, the lateral size of the region is taken as large but finite, i.e., $x \in [-L_x/2; L_x/2]$. Scaling the two spatial coordinates and time as $(x, z, t) = (X, Z, T)/(L_x, L_z, \tau)$, where the time of flight in the cavity is $\tau = nL_z/c$, the resulting equations read

$$(\partial_t \pm \partial_z) E_{\pm} = i\Delta_0 \partial_x^2 E_{\pm} + [i\psi(x, z) - \alpha_i] E_{\pm} + iP_{\pm}(1)$$

$$\partial_t N_0 = J(x, z) - R(N_0) + \mathcal{D} \partial_x^2 N_0 \quad (2)$$

$$- i(P_+ E_+^* + P_- E_-^* - c.c.),$$

$$\partial_t N_{\pm 2} = -[R'(N_0) + 4\mathcal{D}_0 q_0^2] N_{\pm 2} \quad (3)$$

$$- i(P_{\pm} E_{\mp}^* - E_{\pm} P_{\mp}^*),$$

$$R(N) = AN + BN^2 + CN^3. \quad (4)$$

where α_i takes into account for the internal losses that we assume constant for the sake of simplicity, $\psi(x, z) \in \mathbb{R}$ describes the lateral index guiding profile in the weak guiding approximation. The spatially dependent pump current profile is $J(x, z)$. For the sake of simplicity, we restrict our analysis to case where the current stripe possesses a constant transverse width, index and current profiles, i.e. $J(x, z) = J(x)$ and $\psi(x, z) = \psi(x)$. The optical wave vector along the propagation direction z in the medium is $q_0 = 2\pi n/\lambda_0$, and we have defined the scaled diffusion and diffraction lengths are $\mathcal{D} = \tilde{\mathcal{D}} L_x^{-2}$ and $\Delta_0 = \lambda_0/(4\pi n_g) L_z L_x^{-2}$ respectively, with λ_0 the wavelength in vacuum and n and n_g being the effective index and the effective group index. The scaled index guiding profile ψ is related to the waveguide structure by the relation $\psi(x, z) = (q_0 L_z) (\delta n(x, z)/n_g)$ and it is typically an order one quantity even when $\delta n \sim 10^{-3}$. For the sake of simplicity we have neglected the transverse diffusion (i.e. $\mathcal{D} \partial_x^2 N_2$) of the longitudinal population grating N_2 at half the optical wavelength λ_0 since the actual decay rate $4\mathcal{D} q_0^2 \sim 10^{12} \text{ s}^{-1}$ corresponds to a length well below the diffusion length. The non linear recombination $R(N)$ is assumed of a cubic form with the fitting parameters A, B and C , and contains contributions from several sources as the non radiative, the radiative and the Auger contributions. The boundary conditions at the left and right facets read in the simplest case of a Fabry-Perot cavity

$$E_+(x, 0, t) = r_l E_-(x, 0, t), E_-(x, L, t) = r_r E_+(x, L, t). \quad (5)$$

The current stripe is defined between $x_{\pm} = \pm \frac{1}{2}$. The discretization in the longitudinal direction is simple and as detailed in [36] we define a uniform mesh along the direction z composed of N_z points separated by a distance $h = N_z^{-1}$, located at abscissae z_j shifted of $h/2$ from the

Symbol	Value	Units	Meaning
λ_0	1.55	μm	Emission wavelength
n	3.75	-	Effective index
Γ	5%	-	Optical confinement factor
R	1/0.5/0.01	-	Facet power reflectivity
τ_c	12.5	ps	Cavity transit time
$2\alpha_i$	15	cm^{-1}	Internal losses
Ω_g	0	GHz	Band-Edge Frequency
$2\chi_0$	1500	cm^{-1}	Gain factor
γ	8×10^{12}	s^{-1}	Polarization decay rate
N_t	1×10^{18}	cm^{-3}	Carrier Density at transparency
\mathcal{D}	20	cm^2s^{-1}	Ambipolar diffusion coefficient
A	1×10^8	s^{-1}	Non radiative recombination
B	7×10^{-10}	cm^3s^{-1}	Spontaneous recombination
C	1×10^{-29}	cm^6s^{-1}	Auger recombination

Table I: Table of the parameters used in the simulations

boundaries $z = (0, 1)$ and defined by

$$z_j = h \left(j - \frac{1}{2} \right) \quad j \in [1, N_z]. \quad (6)$$

With this approach, the boundary conditions are applied at half integer time steps as discussed in the appendix of in [36].

When the dynamics is restricted to the vicinity of the band-gap, as it is the case of BALDs, it is possible to use a Padé approximation to the optical response as in [2, 26]. Upon transforming back to time domain using that $\partial_t \rightarrow -i\omega$, the time domain evolution equation for the polarizations can be written at a given point (x, z) as

$$\begin{aligned} \partial_t P_{\pm} = & - \left(\frac{1}{ib} + i\omega_p \right) P_{\pm} + \frac{\chi - \omega_p a}{ib} E_{\pm} + \frac{a}{b} \partial_t E_{\pm} \\ & + \frac{\partial_N \chi}{ib} N_{\pm 2} E_{\mp}. \end{aligned} \quad (7)$$

where $\chi = \chi(N_0(x, z, t), \omega_p)$ and a and b are given in [2, 26] respectively, with $N = N_0(x, z, t)$. The spatial dependence of a and b arises from that of $N(x, z)$. If not otherwise stated we use the parameters described in Table.1.

III. RATIONAL CHEBYSHEV TRANSFORM

Assuming that the field and the polarization decay to zero in $x = \pm\infty$, and following the notations of [34], we define the finite Rational Chebyshev Transform of order N_x (with $N_x = 2N$ an even number with the notations of [34]) of the field and of the polarization in the transverse

direction as

$$E_{\pm}(x, z, t) = \sum_{n=-N_x/2}^{N_x/2-1} \tilde{E}_{\pm}(n, z, t) \rho_n(x), \quad (8)$$

$$P_{\pm}(x, z, t) = \sum_{n=-N_x/2}^{N_x/2-1} \tilde{P}_{\pm}(n, z, t) \rho_n(x), \quad (9)$$

where the basis set is defined by the complex rational fractions

$$\rho_n(x) = \frac{(ix - 1)^n}{(ix + 1)^{n+1}}. \quad (10)$$

The link between the RCT and the Fourier transform can be revealed by using change of variables $x = \cot(\theta/2)$ which maps the entire real axis $x \in [-\infty, \infty]$ onto $\theta \in [0, 2\pi]$. Noticing that

$$\rho_n(x) = \exp(in\theta) / (1 + ix), \quad (11)$$

we can emphasize the direct link with the Fourier Transform since

$$(1 + ix) E_{\pm}(x, z, t) = \sum_{n=-N_x/2}^{N_x/2-1} \tilde{E}_{\pm}(n, z, t) e^{in\theta}. \quad (12)$$

Consequently, the RCT transform of a function $E(x)$ defined over N_x grid points, the Right Hand Side (RHS) of Eq. 12, can be obtained by simply seeking the discrete Fourier transform of the function $(1 + ix) E(x)$, that is to say the left hand side (LHS) of Eq. 12, provided that the function $E(x)$ is evaluated over the specific non uniform grid as defined by the $x_j = \cot(\theta_j/2)$, with an uniform distribution of the phases θ_j as

$$\theta_j = 2\pi j / N_x \quad , \quad j \in [0, N_x - 1]. \quad (13)$$

This justifies why the RCT is often called a ‘‘Fourier transform in disguise’’ [30]. A great wealth of information on the Chebyshev Transform and the RCT on infinite and semi-infinite intervals can be found in the free resource [30]. Notice that the infinity is included as a point $x_0 = \infty$ and therefore the limiting behavior of the function must be imposed during the transformation, i.e. $(1 + ix_0) E(x_0) = \lim_{x \rightarrow \infty} (1 + ix) E(x) = 0$. As detailed in [35], the completeness and orthogonality of the basis set $\rho_n(x)$ follows from the properties of the Fourier Transform. In the rest of this manuscript we will be representing the spectral transformation of E (let it be either the RCT or the FT) as a tilde operator, i.e. \tilde{E} .

Here the advantage provided by RCT for the problem at hand is that it represents more accurately than the FT, for a given order N_x , the functions that are localized around $x = 0$ and which decay smoothly in $x = \pm\infty$. This is due to the fact that the density of mesh points decays with the distance from the origin, see Fig. 1. Since we know beforehand that we are going to deal exclusively

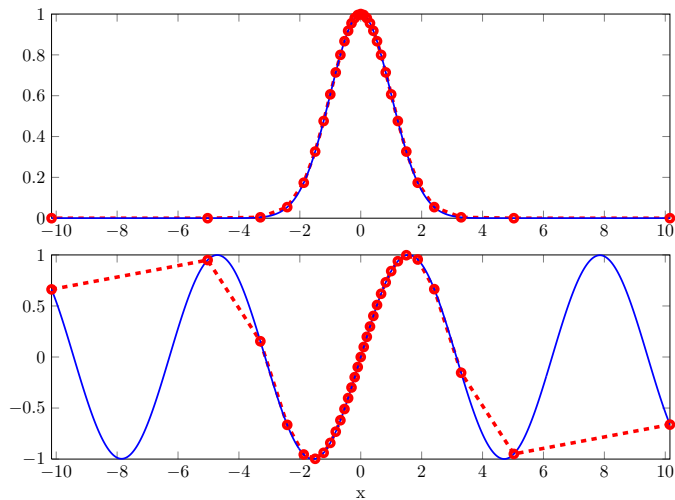


Figure 1: Representation of a localized function $\exp(-x^2/2)$ and a delocalized wave $\sin(x)$ over the non uniform RCT grid width $N_x = 32$.

with such decaying and localized functions, due to the fact that the electrical pumping is localized only over the central stripe, the RCT will prove superior to the FT which is more adapted to represent “delocalized” functions over the whole domain. But it is only by trading the possibility to represent accurately such delocalized functions that we obtain a superior resolution in the vicinity of the current stripe. A neat example of the huge improvement provided in these cases by the RCT is found in Fig. 1 of [37], which compares the convergence of the RCT and of the FT methods in the case of the 1+1 Non Linear Schrödinger equation. Here, the numerical solution obtained with the RCT is indistinguishable from the exact hyperbolic secant with only a handful of mesh points ($N_x = 32$), while the FT method fails qualitatively, by predicting an off-centered, symmetry breaking solution.

IV. INDEX GUIDING AND DIFFRACTION

In order to simplify the notations we will omit the longitudinal and temporal dependence whenever possible. Hence the spectral transformation in the transverse direction of a variable $A(x, z, t)$ will be denoted \tilde{A} instead of $\tilde{A}(n|q, z, t)$ with n the order of the eigenfunction ρ_n for the RCT or q the spatial frequency of the Fourier mode. This has the added benefit of allowing to treat both spectral transformations simultaneously. For the RCT, the fundamental relation for the product of the ρ_n disclosed by [35] reads

$$\rho_n(x) \rho_k(x) = \frac{\rho_{n+k}(x) - \rho_{n+k+1}(x)}{2}. \quad (14)$$

a relation that is very similar to the product of two plane waves in the case of the FT. Hence we can deduce a rela-

tion for the RCT of the product of two functions akin to a cyclic convolution between the RCT of the two original functions,

$$\widetilde{\psi E} = \mathbf{P} \tilde{E}, \quad \mathbf{P} = \frac{\mathbf{C}_\psi - \mathbf{C}'_\psi}{2}. \quad (15)$$

The operation can be constructed as a matrix-vector multiplication, where the RCT of the function $\psi(x)$ is converted into $[\mathbf{C}_\psi - \mathbf{C}'_\psi]/2$. The matrix \mathbf{C}_ψ is a circulant Toeplitz matrix whose lines are composed of the Fourier transform of the function $(1 + ix)\psi(x)$ and \mathbf{C}'_ψ corresponds to a circular shift of all the columns of \mathbf{C}_ψ to the left, or identically a circular shift down of all the lines. In the case of a FT, we would simply have $\mathbf{P} = \mathbf{C}_\psi$ but with the lines of \mathbf{C}_ψ composed by the Fourier transform of the function $\psi(x)$. Assuming that the index profile $\psi(x)$ besides being a real valued function is symmetric with respect to the center to the current stripe entails that $\mathbf{P} = \mathbf{P}^t$ which allow for some optimization and to replace half of the multiplications involved in evaluating Eq. 15 by additions.

With respect to other representations, the FT has the obvious advantage that in the basis of the plane waves, the second derivative operator is diagonal, which justifies the success and the efficiency of the so-called split-step methods. In [2], we exploited fully this fact since it allowed us to integrate exactly the traveling wave equations along the spatio-temporal characteristics $s_\pm = z \mp t$. There, we could describe exactly the effect of the differential operator $\exp\left[i(\Delta_0 h) \frac{\partial^2}{\partial x^2}\right]$ for relatively large values of the step ($h \sim 0.1$) using the so-called Exponential Differentiation. This allowed the decimation method [1] to be extended to the case of transverse diffractive dynamics. In the RCT basis, the second derivative operator is not that simple and following the derivation of [34] (notice a typo in the original derivation of [35]) we have that

$$\frac{\partial^2}{\partial x^2} E_\pm(x, z, t) = \sum_{n=-N_x/2}^{N_x/2-1} \tilde{E}_\pm^{(2)}(n, z, t) \rho_n(x), \quad (16)$$

with the following expression of the coefficients $\tilde{E}_\pm^{(2)}(n)$

$$\begin{aligned} \tilde{E}_\pm^{(2)}(n) = & -\frac{1}{4} \left[n(n-1) \tilde{E}_\pm(n-2) - 4n^2 \tilde{E}_\pm(n-1) \right. \\ & + (6n^2 + 6n + 2) \tilde{E}_\pm(n) - 4(n+1)^2 \tilde{E}_\pm(n+1) \\ & \left. + (n+1)(n+2) \tilde{E}_\pm(n+2) \right], \quad (17) \end{aligned}$$

that is to say

$$\tilde{E}_\pm^{(2)}(n, z, t) = \mathbf{M} \tilde{E}_\pm(n, z, t), \quad (18)$$

where \mathbf{M} is the second order differentiation matrix in the Chebyshev space. Comparing this result to the more standard spectral method based on the FT, we

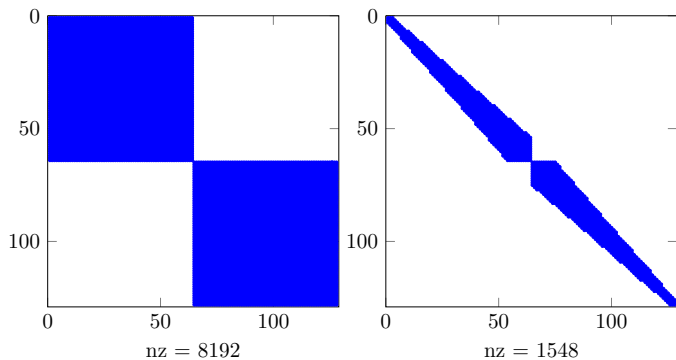


Figure 2: Representation of the exponential of the second order derivative $\mathbf{w}_M = \exp[i(\Delta_0 h)\mathbf{M}]$ with $\Delta_0 h = 3.3 \times 10^{-4}$ (equivalent to a $200 \mu\text{m}$ wide current stripe and a large longitudinal step of $100 \mu\text{m}$) (left) and the same matrix (right) suppressing elements of square modulus smaller than 10^{-8} . The number of non zero elements nz is strongly reduced. Here $N_x = 128$.

have here a symmetric penta-diagonal matrix \mathbf{M} instead of a diagonal one. Taking the exponential of the second order derivative operator as in [2] over a segment of length h defines the exponential differential operator $\mathbf{w}_M = \exp[i(\Delta_0 h)\mathbf{M}]$ which is composed of two block diagonal matrices of size $N_x/2$. At this point, one would think that the possible improvements one obtained by using the RCT instead of the FT are going to be mitigated by the fact that taking the second order derivative has a much increased computational cost. Indeed, such cost would be here of $N_x^2/2$ multiplications, instead of N_x in the case of the FT method. However, a plot of the values of the matrix elements of \mathbf{w}_M is instructive.

On notice in Fig. 2 that the elements of \mathbf{w}_M decrease quickly with respect to the diagonal. By enforcing $w_M^{ij} = 0$ whenever $w_M^{ij} < \varepsilon$, we recover a matrix whose structure is banded and symmetric. Such a nice property of the finite second derivative operator \mathbf{w}_M stems from a physical reason. In a BALD ($h\Delta_0 \ll 1$) and an expansion of \mathbf{w}_M in powers of \mathbf{M} converges quickly, which explains the limited bandwidth. In other words, diffraction is only a weak perturbation of the wave propagation in a broad current stripe, which explains that even upon quite large a propagation distance (i.e. exponential differencing) the diffraction operator conserves its bandwidth limited form. Notice that the sparsity of \mathbf{w}_M was not exploited in [37] where the exponential of \mathbf{M} was explicitly considered as a full matrix.

We represent in Fig. 3 the evolution of the average bandwidth of \mathbf{w}_M as a function of the magnitude of the effect of yjr diffraction ($\Delta_0 h$). Typically, for a large longitudinal step, i.e. a length of the characteristic of $100 \mu\text{m}$ ($h = 0.1$ with the parameters of Section V) and an uniform current stripe of width $2L_x$ of 125 , 250 and $500 \mu\text{m}$, i.e. $h\Delta_0 = 8.4 \times 10^{-4}$, 2.1×10^{-4} and 5.2×10^{-5} , the average bandwidth of \mathbf{w}_M is 17 , 10 and 7 with a cut-off value $\varepsilon = 10^{-8}$. Notice that the total multiplication

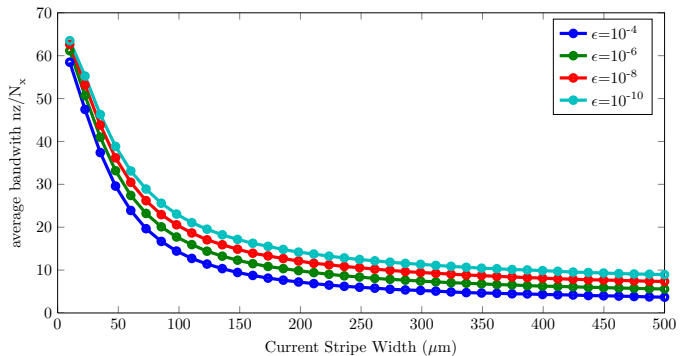


Figure 3: Representation of the average bandwidth of \mathbf{w}_0 as defined by the number of elements whose modulus square is larger than ε divided by the number of lines, for various values of ε . Here $N_x = 128$.

cost involved shall further be divided almost by two using the symmetry $\mathbf{w}_M = {}^t\mathbf{w}_M$, which makes in practice the RCT method almost equivalent in speed as the FT for the operation of taking the exponential of the second derivative. The RCT would get less and less efficient when the current stripe gets narrower. Here, one would think that the FT becomes more adapted. However in such a narrow stripe situation, one would certainly consider a strong index guiding thereby destroying anyway the banded structure. This would also happen with the FT method. Hence, the RCT remains a good choice in all practical situations.

Still, the incurred error due to matrix truncation must remain under control. We discuss in Fig. 4 the error in the operation of taking the exponential of the second derivative due to the ε -truncation of \mathbf{w}_M . We represented e_2 as defined by

$$e_2 = \int_{-\infty}^{\infty} dx |\mathbf{w}_M f(x) - \mathbf{w}_M^\varepsilon f(x)|^2 \quad (19)$$

One notice for instance in Fig. 3 that the value of 10^{-8} retained previously for ε induces an error of 10^{-10} . As expected, such error is of similar order for various functions having similar lateral Full Width at Half Maximum (FWHM) extension.

V. DELAY ALGEBRAIC EQUATION MAPPING

Our method for solving Eqs. (1-4) adapts the DAE approach developed in [1] for the case of a gain guided BALD where we treated exactly the free field equation. Such a method where one integrates exactly some linear contributions has been used in many contexts, sometimes with a great deal of intuition in laser physics as in [24]. It is formally termed Exponential Time Differencing (ETD) [33], although in our case integration is carried out in space-time. The ETD allows to obtain an excellent accuracy through the exact treatment of the stiff linear integrating factors. Here, although the original problem in

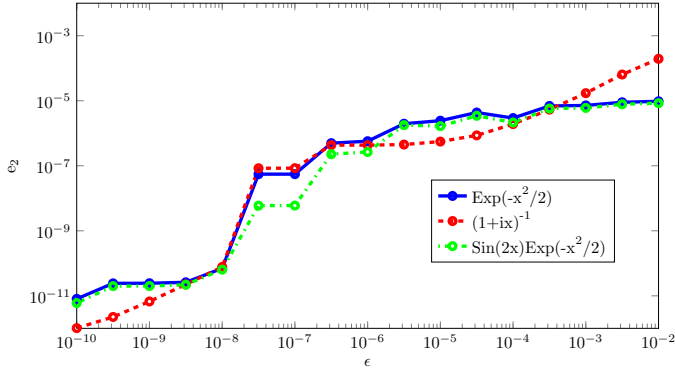


Figure 4: Integral of the square modulus of the difference between the exact and approximated exponential of the second derivative for various functions as a function of the cut-off parameter ϵ . Here $N_x = 128$ and $h\Delta_0 = 3.3 \times 10^{-4}$.

its PDE form is not stiff *per se* along the characteristics, some difficulties are introduced by the spectral transformation. Mainly, the spectral transformation introduces stiffness. This is easier to spot in the simplest case of FT, where the Nyquist mode has a spatial evolution scale proportional to the inverse of its frequency which grows with the transverse mesh size, i.e. $q_N^2 = (\pi/\delta x)^2 \sim N_x^2$. The RCT also gives rise to a second order differentiation matrix of similar stiffness since the eigenvalues of \mathbf{M} increase quadratically from a very small to some very large number, see for instance the discussion regarding the first Figure of [34]. It is why we shall treat exactly the contribution of the stiff linear terms. Such analytical treatment consists in integrating the free field equation over the so-called forward and backward characteristics [25] while performing a linear approximation of the variation of the source term \tilde{P}_\pm which is at the same time a small and a smooth perturbation of the free field propagation, another formulation of the so-called Uniform Field Limit approximation of Laser physics [38].

In a normal spatio-temporal TWM, one must use an identical temporal and longitudinal increment, i.e. $h = \delta t$ in order to fulfill the CFL condition [39]. The DAE approach allows to decouple these two values and to “leapfrog” between spatial points, hence the term of mesh decimation. Such a decoupling is relevant since the temporal increment must be chosen according to the *temporal* stiffness of the active material response, while the spatial increment is related to the gain amplification and to the field *non uniformity* along the characteristics. By analogy with a TWM approach, we define the decimation factor D denoting the number of skipped spatial points as $D = h/\delta t$. When $D = 1$, one recovers the usual TWM, see [1] for details.

In the absence of source $P_\pm = 0$, the general form of the spectral form of the wave equations in the presence of losses and index guiding reads

$$(\partial_t \pm \partial_z) \tilde{E}_\pm(n|q, z, t) = \mathbf{Q} \tilde{E}_\pm(n|q, z, t) \quad (20)$$

with the following definition of \mathbf{Q}

$$\mathbf{Q} = i\Delta_0 \mathbf{M} + i\mathbf{P} - \alpha_i \mathbf{Id}. \quad (21)$$

and of $\mathbf{w}_0(z)$ the free field propagator over an interval z

$$\mathbf{w}_0(z) = \exp(z\mathbf{Q}) \quad (22)$$

Here, we recall that the same formalism can be used either for the RCT or the FT, simply replacing \mathbf{M} by the diagonal matrix of the second derivative in the FT basis $(\frac{\pi}{2})^2 \text{diag}([-N_x/2, \dots, N_x/2 + 1])^2$ and the index guiding matrix \mathbf{P} by \mathbf{C} .

In the presence of an active source, we start by factoring out the influence of the free field propagator by defining

$$\tilde{E}_\pm = \mathbf{w}_0(\pm z) U_\pm \quad (23)$$

hence the wave equation becomes

$$(\partial_t \pm \partial_z) U_\pm = \mathbf{w}_0^{-1}(\pm z) i\tilde{P}_\pm = \mathbf{w}_0(\mp z) i\tilde{P}_\pm. \quad (24)$$

whose integral solution over a characteristics of length h is

$$\tilde{E}_\pm(n, z, t) = \mathbf{w}_0(h) \tilde{E}_\pm(n, z \mp h, t - h) + i\mathcal{S}_\pm, \quad (25)$$

with the following definition of the source \mathcal{S}_\pm

$$\mathcal{S}_\pm = \int_0^h \mathbf{w}_0(h-s) \tilde{P}_\pm(n|q, z \mp h \pm s, t-s) ds \quad (26)$$

As in [2], the source term \mathcal{S}_\pm is approximated by assuming a linear variation of the polarization along the characteristics, i.e. we assume that the distance h between the two points is short enough for the UFL to hold. As such we have, up to third order in h

$$\begin{aligned} \mathcal{S}_\pm &\simeq \mathbf{w}_1 P_\pm(n, z \mp h, t - h) \\ &+ \mathbf{w}_2 [P_\pm(n, z, t) - P_\pm(n, z \mp h, t - h)] \end{aligned} \quad (27)$$

with

$$\mathbf{w}_1 = \int_0^h ds e^{(h-s)\mathbf{Q}}, \quad (28)$$

$$\mathbf{w}_2 = \int_0^h ds e^{(h-s)\mathbf{Q}} \left(\frac{s}{h} \right). \quad (29)$$

The temporal evolution of the field and polarization is therefore given by

$$\begin{aligned} \tilde{E}_{(\pm),j}^{l+1} &= \mathbf{w}_0 \tilde{E}_{(\pm),j\mp 1}^l + i\mathbf{w}_1 \tilde{P}_{(\pm),j\mp 1}^l \\ &+ i\mathbf{w}_2 \left(\tilde{P}_{(\pm),j}^{l+1} - \tilde{P}_{(\pm),j\mp 1}^l \right), \end{aligned}$$

For the evolution of the forward (resp. backward) field on the first (resp. last) point, located at a distance $h/2$ from the boundaries $z = 0$ and $z = 1$ respectively, the coefficients must be integrated over half an interval which is obtained simply by replacing h by $h/2$ in the equations (22,28,29). The practical evaluation of the expressions given by Eqs. (28,29) is discussed in the appendix.

A. Boundary conditions

Since the field are propagated toward the boundaries in direct space, it is trivial to introduce reflection and or transmission coefficient that depend on the longitudinal coordinate in order for instance to model the effect of a diaphragm on the cavity. We present the result of such an approach in Fig.5 where the reflectivity drops to 0 outside of the stripe defined in the interval $x \in [-1; 1]$. The dynamics obtained here is very similar to the zipper state present in the case of gain guided devices. Due to the drop of reflectivity outside of the central region, the FT method performs here as well as the RCT since the high losses induced by the mirror reflectivity profile helps in this particular case confining the field in the central region.

B. Spatio-temporal numerical algorithm

One remarks that the DAE can only be written in the spectral space which is not convenient for the active material description. Hence the methodology consists in transforming back and forth between the direct and the Chebyshev/Fourier space to update the field and the polarization and carriers with the following sequence akin to the pseudo-spectral methods

1. Perform a first order explicit Euler prediction of $\tilde{E}_{\pm}(n|q, z, t + \delta t)$ and transform back to space (x) domain to obtain a first order estimate of $E_{\pm}(x, z, t + \delta t)$.
2. Perform a second order semi-implicit evolution of the polarization and get $P_{\pm}(x, z, t + \delta t)$ as in [26] and perform the spectral transformation in order to get $\tilde{P}_{\pm}(n|q, z, t + \delta t)$.
3. Perform the second order semi-implicit evaluation of $\tilde{E}_{\pm}(n|q, z, t + \delta t)$ as in [26] and transform back to space (x) domain to get $E_{\pm}(x, z, t + \delta t)$.
4. By using a staggered grid for the population inversion (see the appendix of [36] for instance), the carrier equations eqs. (2-3) are treated as in [26]. Here, the effect of carrier diffusion although not critical must be treated in the spectral space due to the non uniform grid if one uses the RCT.

VI. EXAMPLE AND CONVERGENCE PROPERTIES

The longitudinal length of all devices is fixed to the value of 1 mm which leads to a single trip of $\tau_c = 12.5$ ps and to a longitudinal mode spacing of 40 GHz. The temporal increment is $\delta t = \tau_c/N_z \sim 48$ fs. In order to test the numerical method described in the previous section, we consider three BALDs of width $W_x = 28 \mu\text{m}$,

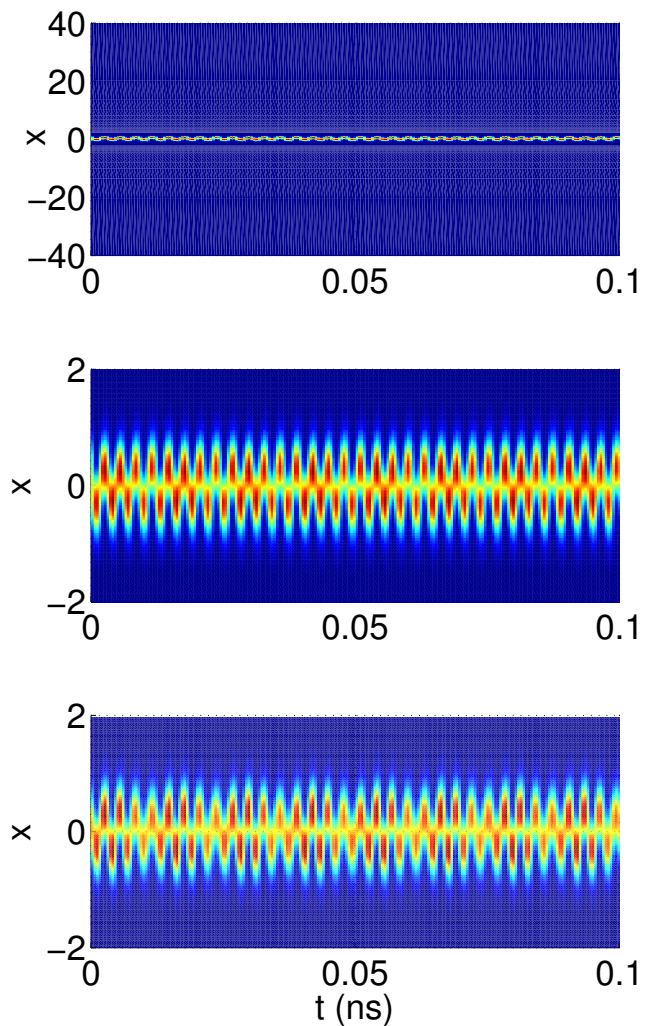


Figure 5: Temporal time trace of the right facet output in the case of a $28 \mu\text{m}$ wide BALD. A zipper state emerge and remains stable up to four times threshold, the current value here is $2.5 J_{th}$. The time traces correspond to the near field intensity pattern on the right facet, i.e. $|E_+(x, 1, t)|^2$ after a 25 ns simulation time. The top line corresponds to the full domain with the RCT method, while the central panel is a zoom on the central region of the stripe. An excellent agreement between the RCT approach (top/center) and the case of the FT method (bottom) is found but in this latter case, the full numerical domain is shown. In all cases, the parameters are $N_x = 128$ and $D = 16$. The mirror reflectivity drops to 0 outside the region $x \in [-1, 1]$.

$W_x = 57 \mu\text{m}$ and $W_x = 114 \mu\text{m}$. As noted before the lateral extent of the integration domain in the case of the FT is $L_x = 2W_x$ while for the RCT it is much larger and increases with N_x as $\sim 2N_x/\pi$ while keeping 50% of the mesh point inside a domain of width W_x . We assume typical values for the semiconductor material as detailed in Table 1. In addition, we fixed the longitudinal mesh size to be $N_z = 257$. Such a convenient value allows us to use decimation factors $D = (128, 64, 32, 16, 8, 4, 2, 1)$.

In addition, if one use power of two for $N_z - 1$ and D , for increasing values of D each mesh is a subset of the previous one which allows restarting the simulation from the previous ones to study the accuracy of the truncation for increasing values of D .

As an initial condition, we use as a transverse profile a Gaussian beam defined as

$$G_a(x, z) = \frac{1}{\sqrt{z - ia}} \exp\left[-\frac{ix^2}{4\Delta_0(z - ia)}\right]. \quad (30)$$

Notice that there is no mistake regarding the presence of the square root in Eq.(30), the standard result in the literature being the solution to the paraxial equation in two dimensions. The main advantage of the Gaussian beam is that it is an eigenfunction of the paraxial equation in the absence of non linear gain and index guiding. Therefore we can use such a profile to compare the numerical and analytical results and study the convergence of both the FT and RCT methods after some integration time. Indeed, if the initial condition is

$$E_+(x, z, 0) = G_a(x, z) \exp(ikz) \quad (31)$$

with $k = m\pi - i \ln(r_l r_r)/2$, a wave-vector solution of the longitudinal propagation problem, after an integer number of round-trip n and therefore a propagation time/length $2n$, the final solution is simply

$$E_+(x, z, 2n) = G_a(x, z + 2n) (r_l r_r)^n \exp(-2n\alpha_i) \quad (32)$$

Here, the advantage of the RCT with respect to the FT method will become quite obvious. We choose as a parameter for the Gaussian beam $a = 10$, which correspond to a well localized profile whose FWHM is equal to $3/4$. Such initial condition was integrated over a single round-trip, i.e. $n = 1$. With $N_x = 64$ the error of the FT method with respect to the analytical result is of the order of 10^{-9} . This is a nice result but looking at how the error is distributed is useful. In Fig. (6), one notices that the field does not reach zero on the lateral side: even if the initial beam was well localized in the cavity, some light will always leak on the sides and experience the folding incurred by the periodic boundary conditions imposed by the FT method. Because of that, increasing N_x does not change the value of the error, preventing any further improvement in the convergence.

On the other hand, the RCT already gives an error of 10^{-19} with $N_x = 64$. This is because in this case the numerical domain is already much broader. Here, the error reduces to 10^{-26} with $N_x = 128$ signaling exponential convergence. This is due to the fact that the numerical domain lateral extension increases with the RCT as $2N_x/\pi$. This explain the widely different behavior we represent in Fig. (7) regarding the convergence of the FT and the RCT methods.

A. Reconstruction

In the case of a large decimation factor the effective mesh along the laser cavity propagation axis is only com-

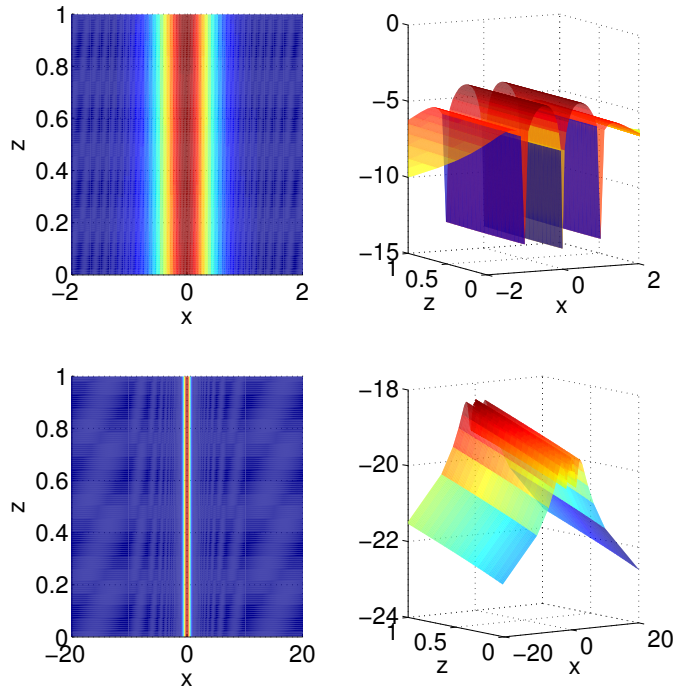


Figure 6: Numerical solution (left) after a single round-trip and deviation (right) from the analytical solution for the Fourier (top) and the Chebyshev (bottom) transforms. For clarity the \log_{10} of the error is represented. Close to the domain boundaries the error is 10^{-6} and 10^{-21} for the FT and the RCT, respectively. The horizontal interval $[-1, 1]$ corresponds to $W_x = 57 \mu\text{m}$.

posed of a few transverse slices. Still, all the complexity of the dynamics remains intact and is hidden in the past values of the field kept at each transverse slice. For instance, it is still possible to reconstruct the full two dimensional profile by using the past values of the fields in order to say, have a intuitive idea of the two dimensional beam profile. Such a reconstruction at a point z_i is done from a past value t_p at the closest point on the left z_l (resp. right z_r) for the forward (resp. backward) propagating wave and reads

$$\begin{aligned} \tilde{E}_{\pm}(n|q, z_i, t) &= \mathbf{w}_0^{\pm}(z_{l,r}, z_i) \tilde{E}_{\pm}(n|q, z_{l,r}, t_p) \\ &+ \mathbf{w}_1^{\pm}(z_{l,r}, z_i) \tilde{P}_{\pm}(n|q, z_{l,r}, t_p) \end{aligned} \quad (33)$$

with $t_p = |z_i - z_{l,r}|$. This spatial reconstruction of the longitudinal profiles of the fields achieved in Eq. (33) is simply an Euler prediction (from the point of view of the source term) to recover the corresponding “missing” transverse slices. The result of such a reconstruction is exemplified in Fig. 8 in the case of a BALD operated in a chaotic regime and where the dynamics is multimode in both the longitudinal and transverse dimensions. The smoothness of the reconstructed profiles indicates *a posteriori* that no significant information was lost. Here, in the case of a large decimation factor the effective

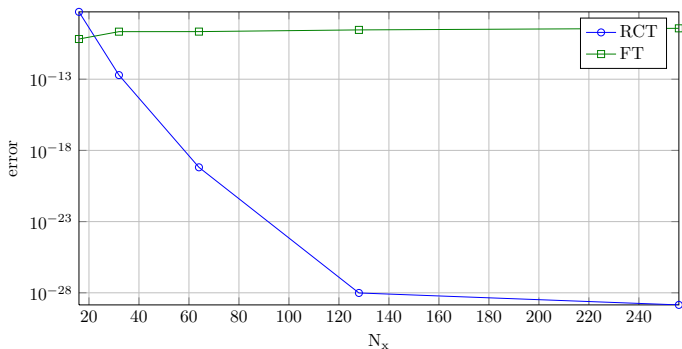


Figure 7: Integral of the square modulus of the error between the exact and the numerical solution after a single trip in the cavity starting with a Gaussian transverse profile with $a = 10$ as an initial condition. Increasing the mesh size does not improve on the accuracy of the FT method due to the non vanishing value of the field close to the periodic boundary condition. On the contrary, the RCT exhibits exponential convergence due to the linear increase of the numerical domain with N_x .

mesh along the laser cavity is only composed of a few slices. Notwithstanding, all the complexity of the dynamics remains intact and is hidden in the past values of the field kept at each slice point and a reconstruction can be achieved using the past values of the fields. Such a reconstruction was discussed in [2] in the case of the FT method in the absence of index guiding. We show in Fig. 8 that the same principle applies also to the presence of index guiding and for the RCT method. The result of such a reconstruction is exemplified in Fig. 8 in the case of a straight, $500\ \mu\text{m}$ wide BALD operated in a chaotic regime and where the dynamics is multimode in both the longitudinal and transverse dimensions. The smoothness of the reconstructed profiles indicates *a posteriori* that no significant information was lost. We started from a noisy initial condition and the snapshot was obtained after 1.25 ns of simulation time, i.e. during the strongly multimode turn-on transient.

B. Mode with index guiding

In the absence of source, we have for a mode E_+

$$E_+(x, z, t) = \Lambda(x) \exp[i(kz - \omega t)], \quad (34)$$

with k one of the possibly complex wave-vector associated with the Fabry-Perot longitudinal modal structure as given by the HelmHoltz equation

$$i(k - \omega) \Lambda = i \left(\Delta_0 \frac{d^2}{dx^2} + n_0 \Theta(x) \right) \Lambda, \quad (35)$$

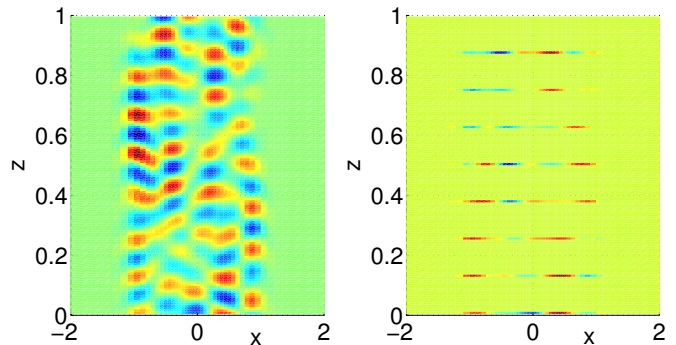


Figure 8: Mesh reconstruction from the past values in the case of a $500\ \mu\text{m}$ long and $57\ \mu\text{m}$ wide device in presence of strong index guiding $n_0 = 3$. Such device support up to 11 confined modes. The decimation factor is $D = 16$ which corresponds to $(N_z - 1)/D = 8$ effective active mesh points. The current is $J = 5J_{th}$ and the facet reflectivities are $(r_l, r_r) = (1, 1)$. Left: real part of the forward field reconstructed from the only 8 active slices (right) in the case of the RCT. Here $N_x = 64$ and the horizontal axis is limited to the central region while the domain extend up to $x \sim \pm 20$.

with Θ the transverse index profile. In the three regions we assume the solution of the form

$$\begin{aligned} \Lambda(x) &= A_l \exp(q_o x), \\ \Lambda(x) &= A_+ \exp(q_+ x) + A_- \exp(q_- x), \\ \Lambda(x) &= A_r \exp(-q_o x), \end{aligned} \quad (36)$$

hence with $\beta = k - \omega$, replacing the ansatz in Eq. (35) gives

$$\beta = \Delta_0 q_0^2 \quad , \quad \beta = \Delta_0 q_{\pm}^2 + n_0, \quad (37)$$

while the field continuity gives in ± 1 defines the dispersion relation

$$1 = \frac{q_+ + q_0}{q_+ - q_0} \frac{q_- - q_0}{q_- + q_0} \exp[2(q_+ - q_-)]. \quad (38)$$

Such a non linear eigenvalue problem can also be solved numerically form a finite size system. Taking the FT or the RCT of Eq. (35) yields

$$(\Delta_0 \mathbf{M} + n_0 \mathbf{P}) \tilde{\Lambda} = \beta \mathbf{Id} \tilde{\Lambda}. \quad (39)$$

hence one simply needs to diagonalize such a matrix. From the inverse spectral transform of the eigenvectors, the profiles of the finite size numerical modes are found. We compare in Fig. (9) the difference between the result given by the finite size system with the analytical solution as defined by Eq. (38). In this respect, the eigenvalues of the finite size system as defined by Eq. (39) gives us an excellent guess as a starting point in order to solve Eq. (38). The error is defined as the integral of the square modulus of the difference between the numerical system of finite size N_x and the analytical result that stem from

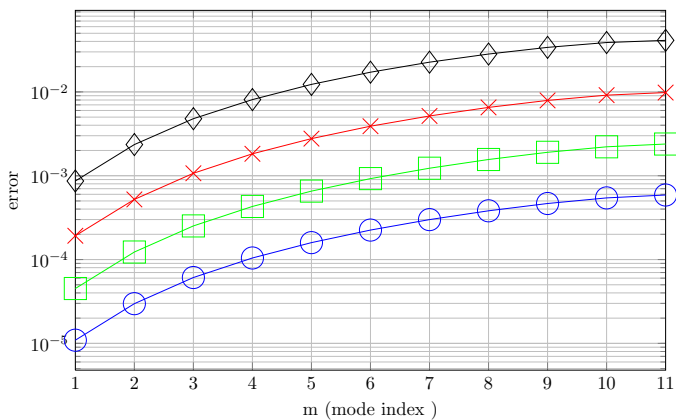


Figure 9: Integral of the square modulus of the error between the numerical and analytical profile for increasing transverse mode index number. The diamond, cross, square and circles correspond to $N = 128, 256, 512$ and 1024 , respectively. The width of the index guiding region is $W_x = 114 \mu\text{m}$.

solving Eq. (35,36,38), i.e.

$$e = \int_{-\infty}^{\infty} |\Lambda_{N_x} - \Lambda^*|^2 dx \quad (40)$$

Inspecting the result in Fig. (9) indicates that the error increases with the mode number which is reasonable due to the larger number of oscillations of the transverse profile for high index values. However, the value of the error with respect to the analytical solution is much larger than for the case where only diffraction is present. This is a well known fact and stem from the presence of a discontinuity. Here, the abrupt variation of the refractive index profile impedes the spectral method of achieving exponential convergence. A separate plot of the convergence properties of a single mode as depicted in Fig.(10) shows only quadratic convergence which is still a good result.

We used large values of the refractive index jump ($n_0 = 3$) in order to have a large number of confined modes (here $m_{max} = 11$). As such the beam profiles are well localized in the center of the numerical domain which explains why we obtained very similar results regarding the convergence properties and the error values for both the FT and the RCT methods. It is however foreseeable that the FT method would be inferior in the case of weak guiding.

VII. CONCLUSION

We presented in this manuscript an unified description that allows using both the Fourier and the Rational Chebyshev spectral method in combination with the decimation method [1] in presence of index guiding and non linear gain guiding. We also pointed out that a non linear adaptive grid can be used with almost no penalty via

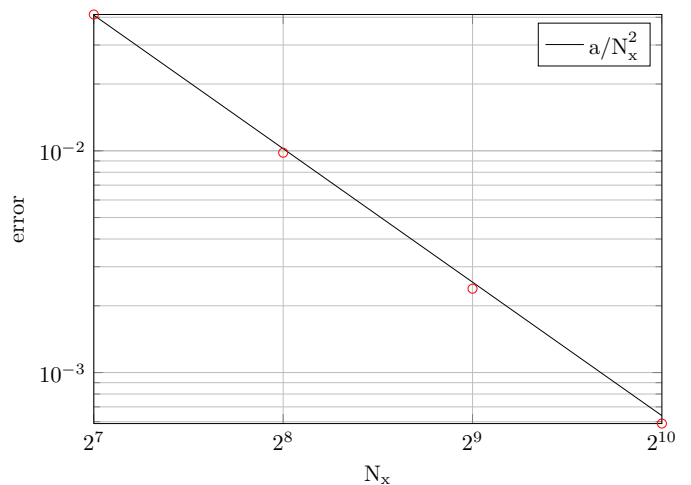


Figure 10: Integral of the square modulus of the error between the numerical and analytical profile for mode number = 11 as a function of the number of mesh point N_x and best fit with a quadratic law.

the Chebyshev approach. Because they are defined on an infinite domain the Chebyshev Rational function set allows handling the boundary conditions with higher accuracy than with the previously studied Fourier Transform method. This improvement is achieved at a negligible cost since the Chebyshev transform is merely a Fourier transform in disguise. However, upon exponentiation of the free field propagator, the Chebyshev approach has the detrimental effect of leading to full matrices. We discussed how by inserting a cut-off upon the matrix element values one can recover a banded sparse matrix. We exemplified our by solving for the beam propagation dynamics in index guiding and tapered gain guided configuration. We obtained excellent result and an improvement of the integration time between one and two orders of magnitudes as compared with a fully distributed two dimensional method, which may alleviate in some cases the necessity of using complex parallel codes. Our approach can be readily extended to other descriptions of the active medium and for instance to the time domain convolution kernel recently developed in [40, 41]. Another important improvement of the method discussed would consider the inclusion of the thermal and electro-thermal effects [42] due to current injection and field two photon absorption which are known to play a dominant role in the dynamics of BALDs. Last but not least, distributed feedback in the weak coupling approximation and assuming uniformity of the coupling in the transverse plane can be readily implemented as in [28].

Acknowledgment

J.J. acknowledges fruitful discussions with A. Perez-Serrano as well as financial support from the Ramon y Cajal fellowship. J.J. and S.B. acknowledge project

funding from project RANGER (TEC2012-38864-C03-01) and from the Direcció General de Recerca, Desenvolupament Tecnològic i Innovació de la Conselleria d'Innovació, Interior i Justícia del Govern de les Illes Balears co-funded by the European Union FEDER funds.

Appendix

An analytical expression can be obtained for the integration weights \mathbf{w}_1 and \mathbf{w}_2 ,

$$\mathbf{w}_1 = \mathbf{Q}^{-1}(\mathbf{w}_0 - \mathbf{I}), \quad (41)$$

$$\mathbf{w}_2 = \mathbf{w}_1 - \mathbf{Q}^{-1}\left(\mathbf{w}_0 - \frac{\mathbf{w}_1}{h}\right). \quad (42)$$

Notice that in the worst case with no losses and no index guiding, the matrix \mathbf{Q} which reduces to \mathbf{M} does not possess any zero eigenvalue, see theorem 6 for (29) in [34], which always ensure the existence of full rank inverse \mathbf{Q}^{-1} and the validity of Eqs. (41,42) in the case of the RCT. The Eqs. (41,42) are also well behaved in the case with the FT but a special treatment must be considered for the case of the zero eigenvalue corresponding to the constant transverse mode $q_x = 0$.

Noteworthy, even if the formal expressions given by Eqs. (41,42) are correct, they shall not be evaluated numerically using the inverse \mathbf{Q}^{-1} which can be numerically unstable. In the case of a purely diffractive case, in general, a power expansion would yield a dangerous method to evaluate a matrix exponential, see [43] for review on the matrix exponential and the discussion on the possibility of a catastrophic cancellation. Notwithstanding, we found the Taylor expansion to work well for our particular problem —when there is no index guiding.— and

to converge after only a few terms, some feature which we attribute mainly to the small values of the $(\Delta_0 h)$ pre-factor in the definition of \mathbf{w}_0 . Here, the $\mathbf{w}_{i,j}$ can be conveniently evaluated from their series expansion that read

$$\mathbf{w}_1 = \sum_{n=0}^{\infty} \frac{h^{n+1}}{(n+1)!} \mathbf{Q}^n, \quad (43)$$

$$\mathbf{w}_2 = \mathbf{w}_{1,j} - \sum_{n=0}^{\infty} \frac{h^{n+1}}{(n+2)n!} \mathbf{Q}^n. \quad (44)$$

Very narrow gain stripes and/or large mesh discretization for which $h\Delta_0 \sim N_x^{-2}$ could however be problematic with this simple method.

In the more complex cases with constant losses and transverse index guiding profiles, analytical estimates of $\mathbf{w}_{1,2,j}^{\pm}$ can still be obtained upon diagonalization, still without using any potentially dangerous matrix inversion. This stem from the fact that in this case $\mathbf{w}_0^{\pm}(s) = \exp(s\mathbf{Q}) = \mathbf{K}^{-1} \exp(s\mathbf{D}) \mathbf{K}$ with \mathbf{K} an orthogonal matrix such that $\mathbf{K}^{-1} = {}^t\mathbf{K}$ and \mathbf{D} diagonal. Although \mathbf{Q} is complex, this diagonalization via an orthogonal matrix is always possible because $\mathbf{Q} \sim i(\mathbf{M} + \mathbf{P})$ with both \mathbf{M} and \mathbf{P} real symmetric. The fact that \mathbf{P} is real symmetric is not entirely trivial. We assumed the index profile to be real and symmetric, hence the Fourier transforms of the two functions involved in the construction of \mathbf{P} , either $\psi(x)$ for the FT or $(1+ix)\psi(x)$ for the RCT, are real symmetric, in the latter case because the Fourier transform of $x\psi(x)$, and odd real function, is purely imaginary.

-
- [1] J. Javaloyes and S. Balle. Multimode dynamics in bidirectional laser cavities by folding space into time delay. *Opt. Express*, 20(8):8496–8502, Apr 2012.
- [2] A. Perez-Serrano, J. Javaloyes, and S. Balle. Spectral delay algebraic equation approach to broad area laser diodes. *Selected Topics in Quantum Electronics, IEEE Journal of*, PP(99):1–1, 2013.
- [3] P. Crump, G. Erbert, H. Wenzel, C. Frevert, C.M. Schultz, K.-H. Hasler, R. Staske, B. Sumpf, A. Maassdorf, F. Bugge, S. Knigge, and G. Trankle. Efficient high-power laser diodes. *Selected Topics in Quantum Electronics, IEEE Journal of*, 19(4):1501211–1501211, July 2013.
- [4] P. Crump, S. Böldicke, C.M. Schultz, H. Ekhteraei, H. Wenzel, and G. Erbert. Experimental and theoretical analysis of the dominant lateral waveguiding mechanism in 975 nm high power broad area diode lasers. *Semicond. Sci. Technol.*, 27:045001, 2012.
- [5] J.P. Leidner and J.R. Marciante. Beam quality improvement in broad-area semiconductor lasers via evanescent spatial filtering. *IEEE J. Quantum Electron.*, 48:1269–1274, 2012.
- [6] G. H. B. Thompson. A theory for filamentation in semiconductor lasers including the dependence of dielectric constant on injected carrier density. *Opto-electronics*, 4:257–310, 1972.
- [7] R.J. Lang, D. Mehuys, A. Hardy, K. M. Dzurko, and D.F. Welch. Spatial evolution of filaments in broad area diode laser amplifiers. *Appl. Phys. Lett.*, 62:1209, 1993.
- [8] I. Fischer, O. Hess, W. Elsässer, and E. Göbel. Complex spatio-temporal dynamics in the near-field of a broad-area semiconductor laser. *Europhys. Lett.*, 35:579–584, 1996.
- [9] C. M. Schultz, P. Crump, H. Wenzel, O. Brox, A. Maassdorf, G. Erbert, and G. Trankle. 11W broad area 976 nm DFB lasers with 58% power conversion efficiency. *Electron. Lett.*, 46:580–581, 2010.
- [10] R.J. Lang, K. Dzurko, A.A. Hardy, S. Demars, and A. Schoenfelder. Theory of grating-confined broad-area lasers. *IEEE J. Quantum Electron.*, 34:2196–2210, 1998.
- [11] K. Paschke, R. Güther, J. Fricke, F. Bugge, G. Erbert, and G. Tränkle. High power and high spectral brightness in 1060 nm α -dfb lasers with long resonators. *Electron. Lett.*, 39:269–270, 2003.
- [12] H. Adachihara, O. Hess, E. Abraham, P. Ru, and P.V.

- Moloney. Spatiotemporal chaos in broad-area semiconductor lasers. *J. Opt. Soc. Am. B*, 10:658–665, 1993.
- [13] J. Martín-Regalado, G. H. M. van Tartwijk, S. Balle, and M. San Miguel. Mode control and pattern stabilization in broad-area lasers by optical feedback. *Phys. Rev. A*, 54:5386, 1996.
- [14] S. K. Mandre, I. Fischer, and W. Elsässer. Spatiotemporal emission dynamics of a broad-area semiconductor laser in an external cavity: stabilization and feedback-induced instabilities. *Opt. Comm.*, 244:355–365, 2005.
- [15] H. Odriozola, J. Tijero, L. Borruel, I. Esquivias, H. Wenzel, F. Dittmar, K. Paschke, B. Sumpf, and G. Ebert. Beam properties of 980-nm tapered lasers with separate contacts: Experiments and simulations. *IEEE J. Quantum Electron.*, 45(1):42–50, 2009.
- [16] M. Spreemann, M. Lichtner, M. Radziunas, U. Bandelow, and H. Wenzel. Measurement and simulation of distributed-feedback tapered master-oscillators power-amplifiers. *IEEE J. Quantum Electron.*, 45:609–616, 2009.
- [17] O. Hess and T. Kuhn. Maxwell-bloch equations for spatially inhomogeneous semiconductor lasers. ii. spatiotemporal dynamics. *Phys. Rev. A*, 54(4):3360–3368, Oct 1996.
- [18] K. Böhrringer and O. Hess. A full-time-domain approach to spatio-temporal dynamics of semiconductor lasers. i. theoretical formulation. *Progress in Quantum Electronics*, 32(5-6):159 – 246, 2008.
- [19] J. Lim, S. Sujecki, L. Lang, Z. Zhang, D. Paboeuf, G. Pauliat, G. Lucas-Leclin, P. Georges, R.C.I. MacKenzie, P. Bream, S. Bull, K.H. Hasler, B. Sumpf, H. Wenzel, G. Erbert, B. Thestrup, P.M. Petersen, N. Michel, M. Krakowski, and E. Larkins. Design and simulation of next-generation high-power, high-brightness laser diodes. *IEEE Journal of Selected Topics in Quantum Electronics*, 15(3):993–1008, 2009.
- [20] U. Bandelow, H. Gajewski, and R. Hünlich. *Optoelectronics Devices - Advanced Simulation and Analysis*, chapter Fabry-Perot lasers: Thermodynamics based modeling, pages 63–85. Springer, New York, 2005.
- [21] R.J. Lang, A.G. Larsson, and J.G. Cody. Lateral modes of broad area semiconductor lasers: theory and experiment. *IEEE J. Quantum Electron.*, 27:312–320, 1991.
- [22] A. E. Siegman. Laser beams and resonators: The 1960s. *IEEE J. Sel. Top. Quantum Electron.*, 6:1380–1388, 2000.
- [23] S. Blaaberg, P.M. Petersen, and B. Tromborg. Structure, stability, and spectra of lateral modes of a broad-area semiconductor laser. *IEEE J. Quantum Electron.*, 43:959–973, 2007.
- [24] J. A. Fleck. Emission of pulse trains by Q -switched lasers. *Phys. Rev. Lett.*, 21(3):131–133, Jul 1968.
- [25] J. A. Fleck. Ultrashort-pulse generation by Q -switched lasers. *Phys. Rev. B*, 1(1):84, Jan 1970.
- [26] J. Javaloyes and S. Balle. Emission directionality of semiconductor ring lasers: A traveling-wave description. *Quantum Electronics, IEEE Journal of*, 45(5):431–438, May 2009.
- [27] J. Javaloyes and S. Balle. Mode-locking in semiconductor Fabry-Pérot lasers. *Quantum Electronics, IEEE Journal of*, 46(7):1023 –1030, july 2010.
- [28] J. Javaloyes and S. Balle. Freetwm: a simulation tool for multisection semiconductor lasers. <http://onl.uib.es/software>, 2012.
- [29] William H. Press, Saul A. Teukolsky, William T. Vetterling, and Brian P. Flannery. *Numerical Recipes: The Art of Scientific Computing*. Cambridge University Press, August 2007.
- [30] John P. Boyd. *Chebyshev and Fourier Spectral Methods*. Springer-Verlag, New York, 1989. 792 pp.
- [31] James Cooley and John Tukey. An algorithm for the machine calculation of complex fourier series. *Mathematics of Computation*, 19(90):297–301, 1965.
- [32] M. Frigo and S. G. Johnson. The fastest Fourier transform in the west (FFTW), release 3.2. <http://www.fftw.org>.
- [33] S.M. Cox and P.C. Matthews. Exponential time differencing for stiff systems. *Journal of Computational Physics*, 176(2):430 – 455, 2002.
- [34] J.A.C. Weideman. The eigenvalues of hermite and rational spectral differentiation matrices. *Numerische Mathematik*, 61(1):409–432, 1992.
- [35] C. I. Christov. A complete orthonormal system of functions in $l_2(-\infty, \infty)$ space. *SIAM Journal on Applied Mathematics*, 42(6):pp. 1337–1344, 1982.
- [36] A. Pérez-Serrano, J. Javaloyes, and S. Balle. Bichromatic emission and multimode dynamics in bidirectional ring lasers. *Phys. Rev. A*, 81(4):043817, Apr 2010.
- [37] I. Towers and Z. Jovanoski. Application of rational chebyshev polynomials to optical problems. *ANZIAM Journal*, 50(0), 2008.
- [38] L.M. Narducci and N. B. Abraham. *Laser Physics and Laser Instabilities*. World Scientific, Singapore, 1988.
- [39] R. Courant, K. Friedrichs, and H. Lewy. Über die partiellen differenzgleichungen der mathematischen physik. *Mathematische Annalen*, 100(1):32–74, 1928.
- [40] J. Javaloyes and S. Balle. Quasiequilibrium time-domain susceptibility of semiconductor quantum wells. *Phys. Rev. A*, 81(6):062505, Jun 2010.
- [41] J. Javaloyes and S. Balle. Detuning and thermal effects on the dynamics of passively mode-locked quantum-well lasers. *Quantum Electronics, IEEE Journal of*, 48(12):1519 –1526, dec. 2012.
- [42] U. Bandelow, M. Radziunas, A. Vladimirov, B. Huettl, and R. Kaiser. Harmonic mode-locking in monolithic semiconductor lasers: Theory, simulations and experiment. *Unpublished*, 2005.
- [43] C. Moler and C. Van Loan. Nineteen dubious ways to compute the exponential of a matrix. *SIAM Review*, 20:801–836, 1978.